Opto-Electronic Advances

ISSN 2096-4579 CN 51-1781/TN

# Highly enhanced UV absorption and light emission of monolayer $WS_2$ through hybridization with $Ti_2N$ MXene quantum dots and g-$C_3N_4$ quantum dots

Anir S. Sharbirin, Rebekah E. Kong, Wendy B. Mato, Trang Thu Tran, Eunji Lee, Jolene W. P. Khor, Afrizal L. Fadli and Jeongyong Kim

**Citation:** Sharbirin AS, Kong RE, Mato WB, et al. Highly enhanced UV absorption and light emission of monolayer $WS_2$ through hybridization with $Ti_2N$ MXene quantum dots and g-$C_3N_4$ quantum dots. *Opto-Electron Adv* **7**, 240029(2024).

https://doi.org/10.29026/oea.2024.240029

Received: 8 February 2024; Accepted: 11 May 2024; Published online: 28 June 2024

Opto-Electronic Advances

Article

June 2024, Vol. 7, No. 6

DOI: 10.29026/oea.2024.240029

# Highly enhanced UV absorption and light emission of monolayer $WS_2$ through hybridization with $Ti_2N$ MXene quantum dots and g-$C_3N_4$ quantum dots

Anir S. Sharbirin, Rebekah E. Kong, Wendy B. Mato, Trang Thu Tran, Eunji Lee, Jolene W. P. Khor, Afrizal L. Fadli and Jeongyong Kim*

Two-dimensional (2D) transition metal dichalcogenides (TMD) are atomically thin semiconductors with promising optoelectronic applications across the visible spectrum. However, their intrinsically weak light absorption and the low photoluminescence quantum yield (PLQY) restrict their performance and potential use, especially in ultraviolet (UV) wavelength light ranges. Quantum dots (QD) derived from 2D materials (2D/QD) provide efficient light absorption and emission of which energy can be tuned for desirable light wavelength. In this study, we greatly enhanced the photon absorption and PLQY of monolayer (1L) tungsten disulfide ($WS_2$) in the UV range via hybridization with 2D/QD, particularly titanium nitride MXene QD ($Ti_2N$ MQD) and graphitic carbon nitride QD (GCNQD). With the hybridization of MQD or GCNQD, 1L-$WS_2$ showed a maximum PL enhancement by 15 times with 300 nm wavelength excitation, while no noticeable enhancement was observed when the excitation photon energy was less than the bandgap of the QD, indicating that UV absorption by the QD played a crucial role in enhancing the light emission of 1L-$WS_2$ in our 0D/2D hybrid system. Our findings present a convenient method for enhancing the photo-response of 1L-$WS_2$ to UV light and offer exciting possibilities for harvesting UV energy using 1L-TMD.

**Keywords:** monolayer TMD; $WS_2$; 2D-derived quantum dots; UV absorption; energy transfer

Sharbirin AS, Kong RE, Mato WB et al. Highly enhanced UV absorption and light emission of monolayer $WS_2$ through hybridization with $Ti_2N$ MXene quantum dots and g-$C_3N_4$ quantum dots. *Opto-Electron Adv* **7**, 240029 (2024).

## Introduction

Transition metal dichalcogenides (TMD) such as, molybdenum disulfide, tungsten disulfide ($WS_2$), molybdenum diselenide, and tungsten diselenide, are two-dimensional (2D) layered semiconducting materials with the bandgap energy of visible and infrared light. In monolayer (1L) thickness, these TMD are direct bandgap semiconductors, exhibiting robust light-matter interactions, with the distinct photoluminescence (PL)[1]. 1L-TMDs display low PL quantum yield (PLQY) due to the high density of lattice defects[2–6] and PLQY of 1L-TMD are especially low under ultra-violet (UV) illumination because UV light mostly excites the carriers at so-called band nesting region located between $\Gamma$ and $Q$ points of the 1st Brillouin zone, which mostly decay non-radiatively before reaching to the $K$ point where the bandgap transition occurs[7,8]. Extensive studies have been carried

Department of Energy Science, Sungkyunkwan University, Suwon 16419, Republic of Korea.

*Correspondence: J Kim, Email: j.kim@skku.edu

Received: 8 February 2024; Accepted: 11 May 2024; Published online: 28 June 2024

out to improve the PLQY of 1L-TMD with some promising successes[9,10], however the enhancement of PLQY upon UV excitation has rarely been studied, severely hampering the practical use of 1L-TMD in UV optoelectronic devices[11,12].

In recent decades, extensive research has been devoted to zero-dimensional (0D) quantum dots (QD) derived from atomically thin 2D materials, including graphene, MXene, graphitic carbon nitride (GCN), hexagonal boron nitride, and phosphorene[13]. The intriguing optical, electronic, and chemical features of these 2D/QD have enabled a vast array of applications in optoelectronics, photocatalysis, supercapacitors, photovoltaics, biosensors, and energy storage[13–17]. When 2D materials are fragmented down to a few nanometers of lateral sizes, improved and distinct characteristics emerge because of prominent edge and quantum confinement effects, while retaining inherent merits of their 2D precursor[13,14,18]. Furthermore, these 2D material-derived QD feature a larger surface-to-volume ratio, better solubility in both aqueous and nonaqueous solvents, higher tunability in physicochemical properties, increased flexibility to hybridize with other nanomaterials, and the easier doping and functionalization than their native 2D forms[19]. Especially, MXene-derived QD (MQD) and GCN-derived QD (GCNQD) with their intrinsic advantages of environmentally friendly chemical components have been documented to possess exceptional optical properties, notably a broad range of energy absorption down to the deep UV region and efficient blue fluorescence[20,21]. In recent years, the construction of 0D/2D mixed-dimensional hybrid has effectively enhanced the PL intensity of TMD as a consequence of interfacial energy transfer (ET) in the hybrid structures[22,23]. For instance, Yu et al. reported a 13-fold enhancement in the PL intensity of 1L-$WS_2$ dispersed with $CsPbBr_3$ QD under 405 nm laser excitation[22–24]. Su et al. showed an enhanced non-radiative resonant ET efficiency up to 73% for hybridization of 1L-$WS_2$ with carbon QD by varying the level of nitridization under visible laser excitations[25]. Also, Su et al. demonstrated full-color, tunable emission in 1L-$MoS_2$/QD thin films prepared from graphene oxide QD or graphene QD[26]. However, these investigations focused on the optical behavior of 1L-TMD under the illumination using visible-light wavelength ranging from 405 nm to 532 nm. To date, the PL enhancement in 2D TMD by using QD hybridization under UV illumination has not been reported.

In this work, titanium nitride ($Ti_2N$) MQD and GCNQD having efficient UV absorption were independently incorporated into 1L-$WS_2$ to develop 0D/2D hybrid structures. Herein, we take full advantage of the merits of these QD facilitating 1L-$WS_2$ to harvest UV light and boost their inherently low PLQY under UV illumination[7,8], which to our knowledge have not been explored yet. Additionally, the MQD and GCNQD are environmentally friendly, distinguished from conventional inorganic QD making them suitable for various biomedical applications[21,27]. We conclude that the intra-hybrid ET from the donor MQD or GCNQD to the acceptor 1L-$WS_2$ is chiefly responsible for the PL enhancement observed in the 1L-$WS_2$/QD hybrid. Accordingly, we combined the efficient UV response of the QD with the excellent optical properties of 1L-$WS_2$ in the visible range, suggesting a fascinating approach for strengthening the optical performance of 1L-TMD in the UV energy range.

## Experimental

### Preparation of 1L-$WS_2$

High-quality $WS_2$ (HQ graphene) was mechanically exfoliated from bulk $WS_2$. Initially, the 1L-$WS_2$ crystals were stripped from the bulk laminate using a transparent Scotch tape and peeled repeatedly with blue Scotch tape. Afterwards, they were transferred from the blue tape to a polydimethylsiloxane (PDMS) film which was attached to the glass slide, and gently detached after a short rest period to ensure that the 1L-$WS_2$ crystals adhered abundantly to the PDMS film[2,28,29]. Eventually, the 1L-$WS_2$ flakes deposited on top of the PDMS stamp were examined under an optical microscope to locate the 1L-$WS_2$ according to the optical contrast under bright-field illumination.

### Synthesis of MQD and GCNQD

The MQD were prepared from $Ti_2N$ MXene powder using a combination of sonication and hydrothermal methods, as reported by Anir et al[30]. Briefly, $Ti_2N$ MXene powder (1.1 g) was obtained by etching the Al layer from the titanium aluminum nitride ($Ti_2AlN$) MAX phase, which was then mixed with deionized water (10 mL). After that, a few drops of ammonium hydroxide ($NH_4OH$) were added slowly to the mixture and subjected to heating at 100 °C for 6 hours. The resulting mixture was then centrifuged at 10000 rpm and the supernatant of the

$Ti_2N$ MQD was collected. In addition, the GCNQD were synthesized based on the ethanol-thermal treatment approach described by Zhan et al[21]. Concisely, urea precursor (20 g) was heated at 550 °C for 6 h with a ramp rate of 3 °C $min^{-1}$. Subsequently, as-synthesized bulk GCN powder (0.03 g) was dispersed in ethanol (30 mL), and concentrated potassium hydroxide (0.45 mL) was added. Afterwards, the mixture was kept in an oven for 6 h at 180 °C, followed by centrifugation at 12000 rpm. Finally, the as-obtained GCNQD pellet was redispersed in water and filtered using a 0.2 μm syringe filter. The transmission electron microscopy (TEM) image in Fig. S1 shows the size distribution of $Ti_2N$ MQD and GCNQD to be 3.2 nm and 3.5 nm, respectively. We further analyzed the element composition of both QD with X-ray photoelectron spectroscopy (XPS) in Fig. S2.

## Preparation of 1L-$WS_2$/QD hybrid

A few drops of diluted QD, either MQD or GCNQD were dispersed on the cleaned $SiO_2$/Si substrate and dried in the vacuum oven at 100 °C. Subsequently, the thin film of QD formed on the $SiO_2$/Si substrate was scratched using a stainless-steel ruler to create an array of QD-dispersed and clean region without QD. Following that, exfoliated 1L-$WS_2$ were deposited across the QD-dispersed and clean region without QD substrate surfaces using a dry transfer approach. The samples were then thermally treated in a vacuum oven to strengthen the adhesion between the 1L-$WS_2$ and the QD.

## Materials characterizations

The morphologies of the $Ti_2N$ MQD and GCNQD were analyzed using high-resolution TEM (JEM-3010, JEOL) and atomic force microscopy (AFM) (XE-120, Park Systems). Ultraviolet photoelectron spectroscopy (UPS) and XPS were conducted using an ESCALAB 250Xi with a monochromatic Al X-ray line. The UV-Vis absorption and PL spectra of the QD solutions were examined using an absorption spectrometer (Optizen, K Lab) and a fluorescence spectrophotometer (Cary Eclipse, Agilent), respectively. The confocal PL mappings were performed using a lab-built laser confocal microscope upon photoexcitation of 375 nm, 405 nm and 514 nm continuous-wave laser at low excitation powers of approximately 76 μW, 17 μW, and 0.8 μW, respectively, measured at the sample. The laser light was focused using a 100× objective lens (*NA* = 0.95) and guided to a 50 cm long monochromator equipped with a cooled charge-coupled device (CCD) (PIXIS 400, Princeton Instruments). For the optical absorption measurements, a commercial confocal microscope (Alpha-300S, WITec Instrument GmbH) with an inverted 60× objective lens was employed. Epifluorescence images of the hybrid samples were captured using a cooled electron-multiplying CCD

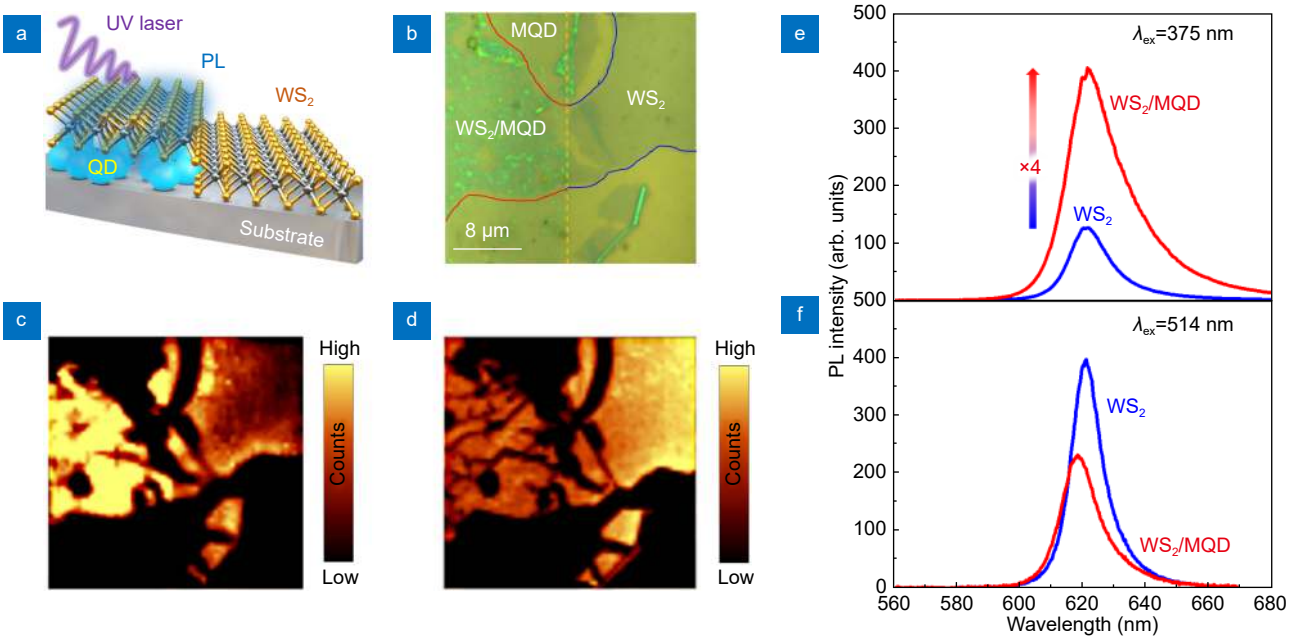


**Fig. 1 |** (**a**) Schematic diagram illustrating the hybrid structure of 2D/QD and 1L-$WS_2$. (**b**) Optical image and (**c**, **d**) Confocal PL mapping images of the 1L-$WS_2$ and 1L-$WS_2$/MQD hybrid obtained with $\lambda_{ex}$ =375 nm and $\lambda_{ex}$ =514 nm, respectively. Scale bar is 8 μm. (**e**, **f**) Representative PL spectra of 1L-$WS_2$/MQD (red curve) and 1L-$WS_2$ (blue curve) with $\lambda_{ex}$ =375 nm and $\lambda_{ex}$ =514 nm.

camera (Photon MAX 512, Princeton Instruments) in a low-light environment with an exposure time of 60 s. A 300 nm UV LED was used as the excitation light source. The UV light was focused using 20×, 0.39 NA micro spot UV focusing objectives and the scattered light was collected using the same objective lens (optical layout of the UV epifluorescence is shown in Fig. S3 in the Supplementary information). The measurement of PL decay lifetime was conducted using the same confocal microscope under the excitation of a 375 nm picosecond pulsed diode laser (BDL-375, Becker & Hickl GmbH). The PL lifetime data were collected using a time-correlated single-photon counting (TCSPC, Becker & Hickl GmbH) correlator. The PL emission of the QD were obtained by selectively filtering out the PL emission from 1L-$WS_2$ in the wavelength range of 560–680 nm using a 550 nm short-pass filter. All optical measurements were conducted at 300 K.

## Results and discussion

### PL characterization of 1L-$WS_2$/MQD hybrid under UV and visible light illuminations

The schematic in Fig. 1(a) illustrates the hybrid of 1L-$WS_2$ and MQD, or GCNQD dispersed on the $SiO_2$/Si substrate. The optical microscope image in Fig. 1(b) shows a 1L-$WS_2$ flake placed across the boundary between the MQD-dispersed and the clean region without MQD on the $SiO_2$/Si substrate. We checked the Raman spectra of our 1L-$WS_2$ (Fig. S4) and the peak difference of 63.9 $cm^{-1}$ between $A_{1g}$ and $E_{2g}$ modes was consistent with the 1L thickness of 1L-$WS_2$[31]. Here 1L-$WS_2$ was exfoliated from bulk $WS_2$ as one piece, and thus, some parts of them were seemingly cracked during the transfer process, but PL characteristics such as the intensity or peak positions of the 1L-$WS_2$ flake shown in the image are expected to be spatially homogeneous. Therefore, any variation in the PL emission of 1L-$WS_2$ across the boundary between the QD region and clean region without QD can be regarded as a result of QD hybridization. Fig. 1(c) and 1(d) display the confocal PL intensity mapping of the same area shown in Fig. 1(b) with two different laser excitation wavelengths ($\lambda_{ex}$) of 375 nm and 514 nm, respectively. Clearly, with $\lambda_{ex}$ = 375 nm, PL intensity of 1L-$WS_2$ is distinctively stronger at 1L-$WS_2$/MQD than at 1L-$WS_2$ without MQD. PL spectra averaged from the entire region of the 1L-$WS_2$/MQD showed a 4.3 times enhancement compared to the 1L-$WS_2$ without MQD hybridization, as shown in Fig. 1(e). The same area of the sample with $\lambda_{ex}$ = 514 nm showed that the PL of 1L-$WS_2$/MQD was somewhat weaker than that of 1L-$WS_2$. The average PL spectra with $\lambda_{ex}$ = 514 nm also confirmed the slight reduction (0.7 times) of the PL intensity of 1L-$WS_2$ upon hybridization with MQD as shown in Fig. 1(f). We inspected several samples in the similar sample configuration and found that the PL of 1L-$WS_2$/MQD was much enhanced with $\lambda_{ex}$ = 375 nm but slightly reduced with $\lambda_{ex}$ = 514 nm(Fig. S5).

### Optical characterization of 1L-$WS_2$/MQD hybrid under 300 nm UV LED illumination

Based on the aforementioned results of the PL enhancement of 1L-$WS_2$ by $\lambda_{ex}$ = 375 nm in Fig. 1, we expected that the PL of 1L-$WS_2$ by MQD hybridization could exhibit even higher PL enhancement if used with a shorter $\lambda_{ex}$ of UV illumination. Figure 2(a) and 2(b) show the optical view of 1L-$WS_2$ flake partly sitting on the dispersed MQD and its epifluorescence image obtained

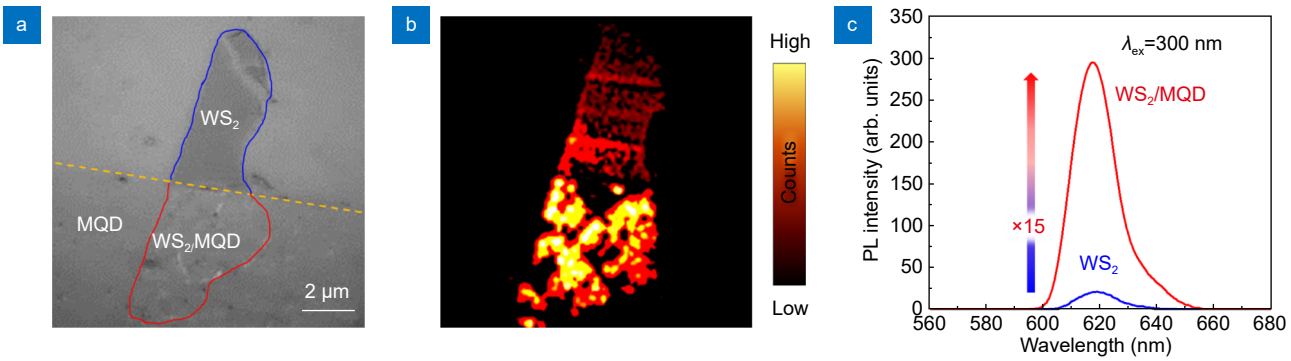


**Fig. 2 |** (**a**) Optical microscope image and (**b**) Epi-fluorescence image of 1L-$WS_2$/MQD hybrid under $\lambda_{ex}$=300 nm UV illumination (orange dotted lines in A indicates the boundary of MQD region and clean region without MQD). Scale bar is 2 μm. (**c**) Representative PL spectra of 1L-$WS_2$/MQD hybrid (red curve) and 1L-$WS_2$ (blue curve) showing a 15-fold enhancement in PL.

with $\lambda_{ex}$ = 300 nm of UV excitation, respectively (the experimental layout of the deep-UV epifluorescence imaging is given in the Supplementary information (Fig. S3)). The PL intensity of 1L-$WS_2$ on MQD was noticeably higher than that on the area without MQD. Figure 2(c) shows that the PL intensity of 1L-$WS_2$/MQD is nearly 15 times higher than that of 1L-$WS_2$ without MQD.

## Optical characterization of 1L-$WS_2$/GCNQD hybrid

In Fig. 3, we show the results of PL mapping of 1L-$WS_2$ hybridized with GCNQD. The confocal PL intensity maps of 1L-$WS_2$ partially sitting on the GCNQD are shown in Fig. 3(a) and 3(b), with two different wavelengths of laser excitation at $\lambda_{ex}$ = 375 nm and $\lambda_{ex}$ =514 nm, respectively. Similar to the results for 1L-$WS_2$/MQD, the PL of 1L-$WS_2$/GCNQD was greatly enhanced compared to 1L-$WS_2$ with $\lambda_{ex}$ =375 nm while the enhancement was not distinct with $\lambda_{ex}$ = 514 nm. A comparison of the average PL spectra also confirmed the same trend of PL enhancement by 3.4 times with hybridization with GCNQD under $\lambda_{ex}$ = 375 nm (Fig. 3(c)), whereas the enhancement was not significant with $\lambda_{ex}$ = 514 nm (Fig. 3(d)). We also used 300 nm wavelength light excitation, as the epi-fluorescence image and PL spectra are shown in Fig. 3(e) and 3(f), respectively, where 1L-$WS_2$/GCNQD exhibited almost 11 times enhancement of PL. We believe that the light absorption by 1L-$WS_2$ in 1L-$WS_2$/QD hybrid is expected to be similar to that of 1L-$WS_2$, thus the observed PL enhancement of 1L-$WS_2$/QD hybrid could be directly interpreted as the enhancement of the PL efficiency or PLQY of 1L-$WS_2$.

## Absorption enhancement of 1L-$WS_2$/MQD and 1L-$WS_2$/GCNQD at UV range

We studied the absorption characteristics to investigate the origin of the PL enhancement observed in 1L-$WS_2$/QD. While the continuous micro absorption spectra of 1L-$WS_2$ or 1L-$WS_2$/QD can be obtained for the visible wavelength range[32], we were able to obtain the absorption at two fixed UV wavelengths by using the fixed wavelength of laser excitation at $\lambda_{ex}$ =300 nm and 375 nm. In Fig. 4, the absorption spectra and data points of 1L-$WS_2$, 1L-$WS_2$/MQD and 1L-$WS_2$/GCNQD are provided that are obtained using the micro-absorption mapping technique[32]. We note that the absorption of 1L-$WS_2$/QD is mostly the same as the absorption of 1L-$WS_2$ for the wavelength longer than 450 nm, then it steeply enhanced compared to the absorption of 1L-$WS_2$ as the wavelength goes into the UV region. The absorption of 1L-$WS_2$/MQD (1L-$WS_2$/GCNQD) obtained at 300 nm

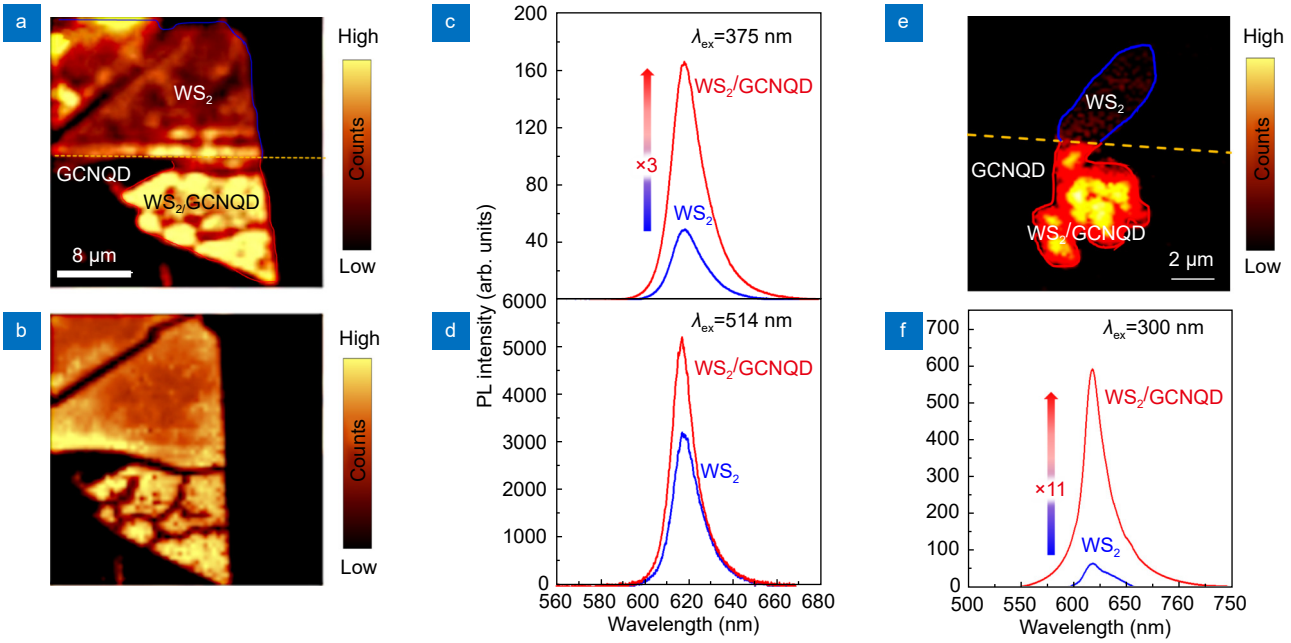


**Fig. 3 |** (**a**, **b**) Confocal PL mapping images of 1L-$WS_2$/GCNQD hybrid with $\lambda_{ex}$ of 375 nm and 514 nm, respectively. Scale bar is 8 μm. (**c**, **d**) Representative PL spectra of 1L-$WS_2$/GCNQD (red curve) and 1L-$WS_2$ (blue curve) with $\lambda_{ex}$=375 nm and $\lambda_{ex}$=514 nm , respectively. (**e**) Epi-fluorescence image of 1L-$WS_2$/GCNQD hybrid with $\lambda_{ex}$=300 nm. (**f**) Representative PL spectra of 1L-$WS_2$/GCNQD (red curve) and 1L-$WS_2$ (blue curve) with $\lambda_{ex}$=300 nm.

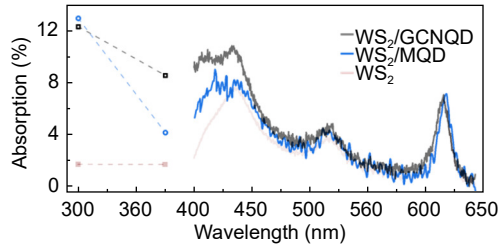


**Fig. 4 | Measured micro absorption spectra of 1L-$WS_2$/GCNQD (black curve), 1L-$WS_2$/MQD (blue curve) and 1L-$WS_2$ only (red curve) as a function of photon wavelength.** Six discrete data points are measured absorptions of 1L-$WS_2$/GCNQD (black), 1L-$WS_2$/MQD (blue) and 1L-$WS_2$ only (red) measured by using laser sources at 300 nm and 375 nm wavelengths. Dashed lines are guides for the eyes.

and 375 nm showed 8.0 (7.6) and 2.6 (5.3) times-increase compared to 1L-$WS_2$, respectively. This increased absorption at UV range is attributed to efficient absorption of UV light by MQD and GCNQD having wide bandgap energies of 3.8 eV[30] and 3.4 eV[33] respectively (Absorption and PL spectra of the MQD and GCNQD are shown in Fig. S6 in the Supplementary information). We believe that the efficient absorption of UV light by QDs in 1L-$WS_2$/QDs hybrids must have contributed to the increase of the PL of 1L-$WS_2$ in 1L-$WS_2$/QDs hybrids through the ET process , as the detailed mechanism of ET is discussed in following section.

## TRPL and energy band alignment of 1L-$WS_2$/QD hybrid

On contrary to the greatly enhanced PL from 1L-$WS_2$ in 1L-$WS_2$/QD hybrid under UV excitation, the PL of MQD and GCNQD in the 1L-$WS_2$/QD hybrid were observed to be significantly quenched by four and three times, respectively, compared to the bare QD as the representative PL spectra are shown in Fig. 5(a) and 5(b). We also obtained time-resolved photoluminescence (TRPL) curves and commonly observed the reduction of PL lifetime of QD, from 1.06 ns to 0.6 ns and from 1.33 ns to 1.0 ns for MQD and GCNQD with hybridization with 1L-$WS_2$, respectively, as shown in Fig. 5(c) and 5(d). Table S1 in the Supplementary information shows the value of short and long components of the decay fitting function. Such PL quenching and reduction of the PL lifetime of QD, together with the PL enhancement of 1L-$WS_2$ for 1L-$WS_2$/QD hybrid upon UV irradiation as discussed above, strongly suggest the occurrence of ET from QD to 1L-$WS_2$ in both of 1L-$WS_2$/MQD or 1L-$WS_2$/GCNQD hybrid upon UV excitation. ET, a non-radiative transfer of energy from one quantum system in excited state (doner) to the other in the ground state (acceptor)

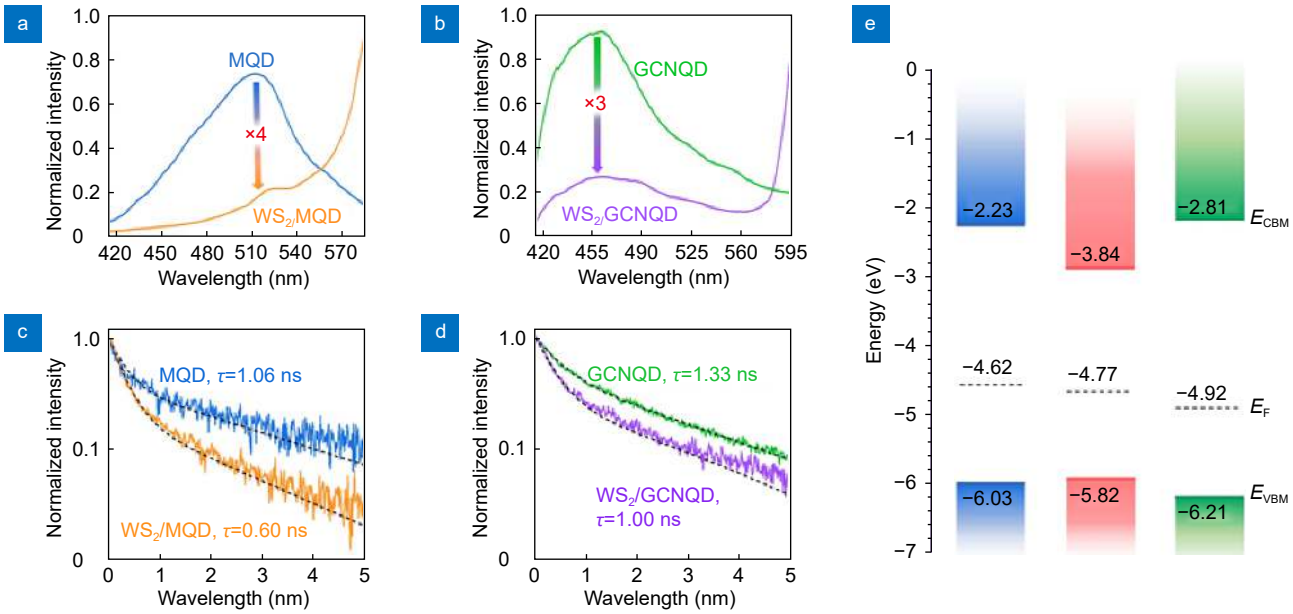


**Fig. 5 |** PL spectra obtained from (**a**) MQD and (**b**) GCNQD in hybrid of 1L-$WS_2$/QD. (**c**) Time-resolved photoluminescence (TRPL) of MQD emission of isolated MQD (blue curve) and 1L-$WS_2$/MQD hybrid (orange curve). (**d**) TRPL of GCNQD emission of isolated GCNQD (green curve) and 1L-$WS_2$/GCNQD hybrid (purple curve) at $\lambda_{ex}$=375 nm. Dotted line represents the fitting curve. The emission of (c) and (d) was collected at the wavelength range of 400-550 nm using the combination of a long-pass filter and a short-pass filter to exclude the emission of 1L-$WS_2$. (**e**) Schematic of energy band alignment showing the type I band alignment of hybrid structure between QD and 1L-$WS_2$. Values of the conduction band minimum ($E_{CBM}$) and the valence band maximum ($E_{VBM}$) and the Fermi level ($E_F$) for each material are marked.

and ET between 1L-TMDs and QDs were previously reported[34] We also observed a slight reduction of PL lifetime of 1L-$WS_2$ emission with hybridization of QD, as the result are shown in Fig. S7 in the Supplementary information. Such reduction of emission lifetime of the acceptor during ET were previously reported[35,36]. Figure 5(e) schematically describes the energy levels of conduction band minimum ($E_{CBM}$) and the valence band maximum ($E_{VBM}$) and the Fermi level ($E_F$) of 1L-$WS_2$[37,38], $Ti_2N$ MQD[30], and GCNQD[33] as estimated from the (UPS) measurement (Fig. S8 in the Supplementary information), bandgap energy estimated from the absorption measurement and the values reported in the literature[39]. Both 1L-$WS_2$/MQD and 1L-$WS_2$/GCNQD are expected to form Type I band alignment between the MQD (or GCNQD) and 1L-$WS_2$[40], and we note that PL spectrum of the MQD (and GCNQD) show considerable spectral overlap with the absorption spectrum of 1L-$WS_2$ as shown in Fig. S9, which is a favorable condition for ET to occur in our 1L-$WS_2$/QD hybrid. Thus, we strongly believe that the significant portion of absorbed energy in MQD and GCNQD in 1L-$WS_2$/QD hybrid under UV irradiation were transferred to 1L-$WS_2$ causing the PL enhancement of 1L-$WS_2$.

In addition to ET, charge transfer (CT) at the interface between 1L-TMD and QD should be also considered because 1L-$WS_2$ and MQD or GCNQD are making a quantum interface and electrons or holes can efficiently transfer across the interface as previously reported in similar 1L-TMD/QD hybrids[41,42], and CT has a major effect on the PL emission of 1L-TMD[24,43], because the PL efficiency of 1L-TMD is heavily affected by excess charge density[44,45]. In 1L-$WS_2$ that is intrinsically n-type[46,47], electron transfer to 1L-$WS_2$ causes an increase in the trion ($A^-$) spectral weight over the neutral exciton ($A^0$). Because $A^-$ tends to decay non-radiatively and has less energy of emission than neutral excitons, increased portion of $A^-$ usually causes an intensity reduction and the red-shift of A peak, respectively[41,48]. We deconvoluted the representative PL spectra of 1L-$WS_2$/MQD and found that under $\lambda_{ex} = 375$ nm, the $A^-$ portion increased from 27% to 45%, suggesting the transfer of electrons from MQD to 1L-$WS_2$ when excited by near-bandgap excitation of MQD ($\lambda_{ex} = 375$ nm). 1L-$WS_2$/GCNQD showed a similar pattern in which the $A^-$ portion was increased from 32% to 45% under$\lambda_{ex} = 375$ nm. (Deconvolution of the PL spectra of 1L-$WS_2$/MQD into $A^0$ and $A^-$ is shown in Fig. S10 in the Supplementary information). The increase of electron density in 1L-$WS_2$ observed from both 1L-$WS_2$/MQD and 1L-$WS_2$/GCNQD is attributed to the CT of photo-excited electrons from QD to 1L-$WS_2$, because the energy of 375 nm wavelength laser light (3.3 eV) is high enough to excite QD and the conduction band of 1L-$WS_2$ is lower than that of $Ti_2N$ MQD or GCNQD. Despite the increased $A^-$ portion of the PL of 1L-$WS_2$ in 1L-$WS_2$/QD hybrid, which generally gives rise to PL quenching[49], we observed a significant increase in the emission intensity under UV illumination. This indicates that the ET from QD to 1L-$WS_2$ is the dominant effect to enhance the PL of 1L-$WS_2$. Considering the efficiency of CT may be controlled by the distance between the doner and acceptor materials, we expect the use of atomic thickness dielectric spacer such as hBN layer could mitigate the CT effect further improving the PL enhancement[50,51].

In order to further investigate the CT in 1L-$WS_2$/QD hybrid, we performed the Raman measurement as the result are shown in Fig. S11 in the Supplementary information. We found that with $\lambda_{ex} = 514$ nm where the photon energy is less than the bandgap of MQD or GCNQD $A_{1g}$ Raman peak in the 1L-$WS_2$/MQD was red-shifted by ~2 $cm^{-1}$, suggesting the increase of electron density in 1L-$WS_2$[52] by hybridization with MQD. For 1L-$WS_2$/GCNQD, slight blue-shift of the $A_{1g}$ peak by ~1 $cm^{-1}$ was detected suggesting the electron depletion of 1L-$WS_2$ by GCNQD. Such n-doping and p-doping effects of 1L-$WS_2$ by MQD and GCNQD suggested from Raman spectra, respectively, are consistent with the increase and decrease of $A^-$ spectral weights of PL spectra taken with $\lambda_{ex} = 514$ nm as shown in Fig. S10. We note that at $\lambda_{ex} = 514$ nm, charge carriers of QD are not excited either in 1L-$WS_2$/MQD or 1L-$WS_2$/GCNQD, limiting the electron transfer from QD to 1L-$WS_2$. Thus, observed variations of PL spectral weights and Raman $A_{1g}$ peak positions are attributed to the CT due to the slight differences in Fermi level between 1L-$WS_2$ and MQD or GCNQD, as shown in Fig. 5(e).

## Conclusion

We showed that hybridization with $Ti_2N$ MQD and GCNQD gave rise to a maximum of 15 times increase in the PL emission of 1L-$WS_2$ for 300 nm wavelength of UV excitation. The observed PL enhancement in the 1L-$WS_2$/QD hybrid strongly suggests the occurrence of ET from the MQD or GCNQD to 1L-$WS_2$ upon UV excitation, as evidenced by TRPL, Raman and PL analysis. The

increase of $A^-$ spectral weight and red-shift of A peak position suggest that the CT also occurred in the 1L-$WS_2$/QD hybrid which can cause the PL quenching under visible light. However, the PL enhancement was still observed because the contribution of increase in absorption and the energy transfer under UV illumination compensated the undesirable CT effect. Because ET and CT are crucially dependent on the alignment of energy bands, use of various kinds of 1L-TMDs to hybridize with MQD or GCNQD can provide diverse characteristics in terms of the enhancement and tunability of light emission from 1L-TMDs, which are to be further investigated in separate studies. Our findings offer an efficient approach for enhancing the UV response of 1L-$WS_2$ with the hybridization using wide-bandgap QD, thus paving the way for the development of next-generation optoelectronic and fluorescence-sensing probe technologies with superior UV light-harvesting performances using 1L-TMD.

## References


1. Mak KF, Lee C, Hone J et al. Atomically thin $MoS_2$: a new direct-gap semiconductor. *Phys Rev Lett* **105**, 136805 (2010).
2. Lee Y, Forte JDS, Chaves A et al. Boosting quantum yields in two-dimensional semiconductors via proximal metal plates. *Nat Commun* **12**, 7095 (2021).
3. Wang HN, Zhang CJ, Rana F. Ultrafast dynamics of defect-assisted electron–hole recombination in monolayer $MoS_2$. *Nano Lett* **15**, 339–345 (2015).
4. Khor JWP, Tran TT, Sharbirin AS et al. Prediction of quantum yields of monolayer $WS_2$ by machine learning. *Adv Opt Mater* **12**, 2302195 (2024).
5. Lee E, Dhakal KP, Song H et al. Anomalous temperature and polarization dependences of photoluminescence of metal-organic chemical vapor deposition-grown $GeSe_2$. *Adv Opt Mater* **12**, 2301355 (2024).
6. Tran TT, Lee Y, Roy S et al. Synergetic enhancement of quantum yield and exciton lifetime of monolayer $WS_2$ by proximal metal plate and negative electric bias. *ACS Nano* **18**, 220–228 (2024).
7. Kozawa D, Kumar R, Carvalho A et al. Photocarrier relaxation pathway in two-dimensional semiconducting transition metal dichalcogenides. *Nat Commun* **5**, 4543 (2014).
8. Hill HM, Rigosi AF, Roquelet C et al. Observation of excitonic rydberg states in monolayer $MoS_2$ and $WS_2$ by photoluminescence excitation spectroscopy. *Nano Lett* **15**, 2992–2997 (2015).
9. Lee Y, Kim J. Controlling lattice defects and inter-exciton interactions in monolayer transition metal dichalcogenides for efficient light emission. *ACS Photonics* **5**, 4187–4194 (2018).
10. Huang XH, Li ZD, Liu X et al. Neutralizing defect states in $MoS_2$ monolayers. *ACS Appl Mater Interfaces* **13**, 44686–44692 (2021).
11. Wang Z, Dong ZG, Gu YH et al. Giant photoluminescence enhancement in tungsten-diselenide-gold plasmonic hybrid structures. *Nat Commun* **7**, 11283 (2016).
12. Huang X, Feng XW, Chen L et al. Fabry-Perot cavity enhanced light-matter interactions in two-dimensional van der Waals heterostructure. *Nano Energy* **62**, 667–673 (2019).
13. Singh KJ, Ahmed T, Gautam P et al. Recent advances in two - dimensional quantum dots and their applications. *Nanomaterials* **11**, 1549 (2021).
14. Xu YH, Wang XX, Zhang WL et al. Recent progress in two-dimensional inorganic quantum dots. *Chem Soc Rev* **47**, 586–625 (2018).
15. Zheng F, Chen Z, Li JF et al. A highly sensitive CRISPR-empowered surface plasmon resonance sensor for diagnosis of inherited diseases with femtomolar-level real-time quantification. *Adv Sci* **9**, 2105231 (2022).
16. Chen Z, Li JF, Li TZ et al. A CRISPR/Cas12a-empowered surface plasmon resonance platform for rapid and specific diagnosis of the Omicron variant of SARS-CoV-2. *Natl Sci Rev* **9**, nwac104 (2022).
17. Xue TY, Liang WY, Li YW et al. Ultrasensitive detection of miRNA with an antimonene-based surface plasmon resonance sensor. *Nat Commun* **10**, 28 (2019).
18. Shao BB, Liu ZF, Zeng GM et al. Two-dimensional transition metal carbide and nitride (MXene) derived quantum dots (QDs): synthesis, properties, applications and prospects. *J Mater Chem A* **8**, 7508–7535 (2020).
19. Wang XW, Sun GZ, Li N et al. Quantum dots derived from two-dimensional materials and their applications for catalysis and energy. *Chem Soc Rev* **45**, 2239–2262 (2016).
20. Xue Q, Zhang HJ, Zhu MS et al. Photoluminescent $Ti_3C_2$ MXene quantum dots for multicolor cellular imaging. *Adv Mater* **29**, 1604847 (2017).
21. Zhan Y, Liu ZM, Liu QQ et al. A facile and one-pot synthesis of fluorescent graphitic carbon nitride quantum dots for bio-imaging applications. *New J Chem* **41**, 3930–3938 (2017).
22. Liu Y, Li H, Zheng X et al. Giant photoluminescence enhancement in monolayer $WS_2$ by energy transfer from $CsPbBr_3$ quantum dots. *Opt Mater Express* **7**, 1327–1334 (2017).
23. Luo Y, Shan HY, Gao XQ et al. Photoluminescence enhancement of $MoS_2$/CdSe quantum rod heterostructures induced by energy transfer and exciton-exciton annihilation suppression. *Nanoscale Horiz* **5**, 971–977 (2020).
24. Boulesbaa A, Wang K, Mahjouri-Samani M et al. Ultrafast charge transfer and hybrid exciton formation in 2D/0D heterostructures. *J Am Chem Soc* **138**, 14713–14719 (2016).
25. Su WT, Li JK, Chen F et al. Enhancing nonradiative energy transfer between nitridized carbon quantum dots and monolayer $WS_2$. *J Phys Chem C* **123**, 25456–25463 (2019).
26. Su WT, Wang YC, Wu WW et al. Towards full-colour tunable photoluminescence of monolayer $MoS_2$/carbon quantum dot ultra-thin films. *J Mater Chem C* **5**, 6352–6358 (2017).
27. Sharbirin AS, Akhtar S, Kim JY. Light-emitting MXene quantum dots. *Opto-Electron Adv* **4**, 200077 (2021).
28. Rigosi AF, Hill HM, Li YL et al. Probing interlayer interactions in transition metal dichalcogenide heterostructures by optical spectroscopy: $MoS_2/WS_2$ and $MoSe_2/WSe_2$. *Nano Lett* **15**, 5033–5038 (2015).
29. Castellanos-Gomez A, Buscema M, Molenaar R et al. Deterministic transfer of two-dimensional materials by all-dry viscoelastic stamping. *2D Mater* **1**, 011002 (2014).

30. Sharbirin AS, Roy S, Tran TT et al. Light-emitting $Ti_2N$ (MXene) quantum dots: synthesis, characterization and theoretical calculations. *J Mater Chem C* **10**, 6508–6514 (2022).
31. Zeng HL, Liu GB, Dai JF et al. Optical signature of symmetry variations and spin-valley coupling in atomically thin tungsten dichalcogenides. *Sci Rep* **3**, 1608 (2013).
32. Dhakal KP, Duong DL, Lee J et al. Confocal absorption spectral imaging of $MoS_2$: optical transitions depending on the atomic thickness of intrinsic and chemically doped $MoS_2$. *Nanoscale* **6**, 13028–13035 (2014).
33. Zhai SC, Guo P, Zheng JM et al. Density functional theory study on the stability, electronic structure and absorption spectrum of small size g-$C_3N_4$ quantum dots. *Comput Mater Sci* **148**, 149–156 (2018).
34. Asaithambi A, Kazemi Tofighi N, Ghini M et al. Energy transfer and charge transfer between semiconducting nanocrystals and transition metal dichalcogenide monolayers. *Chem Commun* **59**, 7717–7730 (2023).
35. Marin DM, Payerpaj S, Collier GS et al. Efficient intersystem crossing using singly halogenated carbomethoxyphenyl porphyrins measured using delayed fluorescence, chemical quenching, and singlet oxygen emission. *Phys Chem Chem Phys* **17**, 29090–29096 (2015).
36. Seo C, Kim M, Lee J et al. Spectroscopic evidence of energy transfer in bodipy-incorporated nano-porphyrinic metal-organic frameworks. *Nanomaterials* **10**, 1925 (2020).
37. Park J, Kim MS, Cha E et al. Synthesis of uniform single layer $WS_2$ for tunable photoluminescence. *Sci Rep* **7**, 16121 (2017).
38. Ma YD, Dai Y, Guo M et al. Electronic and magnetic properties of perfect, vacancy-doped, and nonmetal adsorbed $MoSe_2$, $MoTe_2$ and $WS_2$ monolayers. *Phys Chem Chem Phys* **13**, 15546–15553 (2011).
39. Peng Q, Wang ZY, Sa B et al. Electronic structures and enhanced optical properties of blue phosphorene/transition metal dichalcogenides van der Waals heterostructures. *Sci Rep* **6**, 31994 (2016).
40. Wu LL, Chen YZ, Zhou HZ et al. Ultrafast energy transfer of both bright and dark excitons in 2D van der Waals heterostructures beyond dipolar coupling. *ACS Nano* **13**, 2341–2348 (2019).
41. Roy S, Neupane GP, Dhakal KP et al. Observation of charge transfer in heterostructures composed of $MoSe_2$ quantum dots and a monolayer of $MoS_2$ or $WSe_2$. *J Phys Chem C* **121**, 1997–2004 (2017).
42. Neupane GP, Wang BW, Tebyetekerwa M et al. Highly enhanced light–matter interaction in MXene quantum dots–monolayer $WS_2$ heterostructure. *Small* **17**, 2006309 (2021).
43. Mawlong LPL, Bora A, Giri PK. Coupled charge transfer dynamics and photoluminescence quenching in monolayer $MoS_2$ decorated with $WS_2$ quantum dots. *Sci Rep* **9**, 19414 (2019).
44. Lin JD, Han C, Wang F et al. Electron-doping-enhanced trion formation in monolayer molybdenum disulfide functionalized with cesium carbonate. *ACS Nano* **8**, 5323–5329 (2014).
45. Kim MS, Roy S, Lee J et al. Enhanced light emission from monolayer semiconductors by forming heterostructures with ZnO thin films. *ACS Appl Mater Interfaces* **8**, 28809–28815 (2016).
46. Cao YM, Wood S, Richheimer F et al. Enhancing and quantifying spatial homogeneity in monolayer $WS_2$. *Sci Rep* **11**, 14831 (2021).
47. Bianchi MG, Risplendi F, Re Fiorentin M et al. Engineering the electrical and optical properties of $WS_2$ monolayers via defect control. *Adv Sci* **11**, 2305162 (2024).
48. Mouri S, Miyauchi Y, Matsuda K. Tunable photoluminescence of monolayer $MoS_2$ via chemical doping. *Nano Lett* **13**, 5944–5948 (2013).
49. Bora A, Paul S, Hossain MT et al. Quantitative understanding of the photoluminescence modulation and doping of monolayer $WS_2$ by heterostructuring with Non-van der Waals 2D $Bi_2O_2Se$ quantum dots. *J Phys Chem C* **126**, 12623–12634 (2022).
50. Kim MS, Seo C, Kim H et al. Simultaneous hosting of positive and negative trions and the enhanced direct band emission in $MoSe_2/MoS_2$ heterostacked multilayers. *ACS Nano* **10**, 6211–6219 (2016).
51. Xu WS, Kozawa D, Zhou YQ et al. Controlling photoluminescence enhancement and energy transfer in $WS_2$: hBN: $WS_2$ vertical stacks by precise interlayer distances. *Small* **16**, 1905985 (2020).
52. Haidari MM, Kim H, Kim JH et al. Doping effect in graphene-graphene oxide interlayer. *Sci Rep* **10**, 8258 (2020).

## Acknowledgements

This work was supported by National Research Foundation of Korea (NRF) funded by the Ministry of Education (2021R1A6A1A03039696; 2022R1A2C2009412). Anir S. Sharbirin, Rebekah E. Kong and Wendy B. Mato contributed equally to this work.

## Author contributions

A. S. Sharbirin, R. E. Kong, and W. B. Mato fabricated the samples, performed material and optical characterization, analyzed the data and wrote the manuscript. T. T. Tran, E. J. Lee and J. W. P. Khor performed sample preparation and analyzed the data. J. Y. Kim analyzed the data and wrote the manuscript. All of the authors discussed and commented on the manuscript.

## Competing interests

The authors declare no competing financial interests.

## Supplementary information

Supplementary information for this paper is available at https://doi.org/10.29026/oea.2024.240029